Patch frequencies in rhombic Penrose tilings

Jan Mazáč*

Fakultät für Mathematik, Universität Bielefeld, Postfach 100131, Bielefeld 33501, Germany. *Correspondence e-mail: jmazac@math.uni-bielefeld.de

This exposition presents an efficient algorithm for an exact calculation of patch frequencies for rhombic Penrose tilings. A construction of Penrose tilings via dualization is recalled and, by extending the known method for obtaining vertex configurations, the desired algorithm is obtained. It is then used to determine the frequencies of several particularly large patches which appear in the literature. An analogous approach works for a particular class of tilings and this is also explained in detail for the Ammann–Beenker tiling.

1. Introduction

The idea of a non-periodic tiling of a plane with fivefold symmetry goes back to Kepler's famous Figure Aa (Kepler, 1940). The (rhombic) tiling introduced by Roger Penrose (1974) is an aperiodic fivefold symmetric tiling of a plane with two prototiles – a thick and a thin rhombus. There are many ways to generate this tiling. One can define local matching rules, or one can think of it as an inflation tiling and define inflation rules. A more algebraic approach is due to de Bruijn (1981a,b). It relies on the dualization of a pentagrid, *i.e.* the union of five rotated lattices. An overview of the methods can be found in, for example, Baake & Grimm (2013). Here, we are interested in another algebraic, yet different, approach. It profits from the geometry of the root lattice A_4 and the fact that this lattice is a 'minimal' one with fivefold symmetry. Again, this approach uses dualization, in this scenario the duality relation between Voronoi and Delone cells (and their complexes).

Recently, the rhombic Penrose tiling was considered as an infinite graph and it has been studied using tools from graph theory. One can consider its graph-theoretic properties like Hamiltonicity, Eulericity or (perfect) matchings (Flicker *et al.*, 2020; Lloyd *et al.*, 2022), but one can also assign an operator acting on this graph and study its spectral properties. Damanik *et al.* (2022) studied the properties of a Laplacian on various tilings, among them the rhombic Penrose one. They studied a tile model for the Laplacian and they were able to show some examples of locally supported eigenfunctions, which are also known from other reports (Fujiwara *et al.*, 1988). Recently, Oktel published several papers dealing with a similar problem for the vertex model for different tilings (Oktel, 2021, 2022; Keskiner & Oktel, 2022). For all these models, one can further study the integrated density of states (IDS), which is a function that counts the number of states (different eigenfunctions) up to a given energy. It is known that this function is discontinuous. More precisely, if one can find a locally supported eigenfunction with energy E of the Laplacian, the IDS has a discontinuity jump at point E. The size of this gap is at least as big as the frequency of the eigenfunction's support, *i.e.* the frequency of the corresponding patch (Damanik *et al.*,
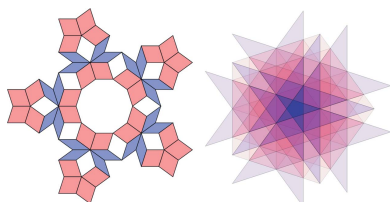
2022). Thus, knowing the frequency, one obtains a lower bound on the size of the gap. Damanik and co-workers used a direct approach to calculate the frequencies, namely, they counted the number of occurrences of the support of a given eigenfunction in growing approximants of the entire tiling. The same method was employed earlier by Fujiwara *et al.* (1988). There is an obvious disadvantage to this method in that one has to deal with the boundary of the approximants, which may include parts of the studied patch. Another problem constitutes the way of choosing the approximants. Lastly, the resulting frequency is always given as a numerical approximation. Therefore, we aim to fill this gap by showing an algebraic way of obtaining the frequencies of arbitrary finite patches in (not only) Penrose rhombic tilings exactly, without any need for the inflation method. For Penrose rhombic tilings, there already exists a method introduced by Zobetz & Preislinger (1990) using de Bruijn's approach, which enables a calculation of the frequencies of vertex configurations in generalized Penrose tilings. Still, our approach provides a more general framework as it allows us effectively to calculate an exact frequency of arbitrary large patches for a wider class of tilings. As far as we are aware, no algorithm yet exists that would actually enable the calculation of exact frequencies for arbitrary finite patches.

This paper is structured as follows. In Section 2, we recall the geometry of the A_4 lattice and its Voronoi complex and of their dual objects. Further, in Section 3, we recall a representation of a cyclic group of order 5 (which acts naturally on the lattice A_4), which exhibits fivefold symmetry in a plane. Section 4 evokes the dualization method and its benefits. These sections are almost fully based on the work of Baake *et al.* (1990). We recall these concepts as they are necessary for the algorithm. The crucial point is that it describes tilings rather than point sets by a variant of the projection method known as dualization. In particular, the standard model set approach via the intersection of translated windows (Baake & Grimm, 2013, Cor. 7.3) is in practice unable to give the frequencies of large patches. The algorithm for determining the frequencies is presented in Section 5. In Appendix *A*, we apply it to several patches coming from the work of Damanik *et al.* (2022). Appendix *B* is devoted to a brief summary of the patch frequencies in Ammann–Beenker tilings.

2. The root lattice A_4, its dual and their properties

The lattice A_4 can be understood in different ways. Perhaps the most natural one (explaining its name) is that A_4 is the root lattice of the semisimple Lie algebra $\mathfrak{sl}_5(\mathbb{C})$. On the other hand, its explicit description as an intersection of the primitive five-dimensional cubic lattice with a four-dimensional (4D) hyperplane allows us to simplify some calculations. Thus, let $\mathbf{e}_1, \ldots, \mathbf{e}_5$ be the standard basis vectors of $\mathbb{R}^5$ and set $\mathbf{s} = \mathbf{e}_1 + \ldots + \mathbf{e}_5$. Further, let $\mathcal{S} = \{\mathbf{x} \in \mathbb{R}^5 \ : \ \mathbf{s} \cdot \mathbf{x} = 0\} \simeq \mathbb{R}^4$ be a four-dimensional hyperplane in $\mathbb{R}^5$. Then, one has

$$A_4 = \mathcal{S} \cap \mathbb{Z}^5. \tag{1}$$

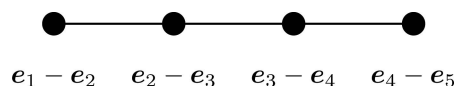The resulting lattice is generated by four vectors, namely

$$A_4 = \langle \mathbf{e}_1 - \mathbf{e}_2, \mathbf{e}_2 - \mathbf{e}_3, \mathbf{e}_3 - \mathbf{e}_4, \mathbf{e}_4 - \mathbf{e}_5 \rangle_{\mathbb{Z}}. \tag{2}$$

Alternatively, we can depict the root lattice A_4 as a Dynkin diagram (Fig. 1).

Note that the generating vectors $\mathbf{e}_i - \mathbf{e}_{i+1}$ are fundamental (or simple) roots of the root system of $\mathfrak{sl}_5(\mathbb{C})$. This system consists of 20 root vectors, namely $\mathbf{e}_i - \mathbf{e}_j$ with $1 \leq i, j \leq 5$ and $i \neq j$. For our further analysis, we need to describe the maximal point symmetry group H_{A_4} at the origin of the lattice A_4. It is isomorphic with the automorphism group of the generating root system. The root system is, by definition, invariant under the action of the Weyl group $W(A_4)$, which is the permutation group S_5 in this case. Moreover, central inversion is an additional symmetry generating the group Z_2. Thus, the group H_{A_4} is isomorphic to

$$H_{A_4} \simeq W(A_4) \times Z_2 \simeq S_5 \times Z_2. \tag{3}$$

The 20 root vectors also determine the Voronoi cell $V_{A_4}(\mathbf{0})$ around the origin, *i.e.* all vectors in the underlying hyperplane $\mathcal{S}$ which are not further away (with respect to the Euclidean distance) from the origin than from any other lattice point, so

$$V_{A_4}(\mathbf{0}) = \left\{ \mathbf{x} \in \mathcal{S} \ : \ \forall \mathbf{v} \in A_4 \ : \ ||\mathbf{x} - \mathbf{v}|| \geq ||\mathbf{v}|| \right\}. \tag{4}$$

The Voronoi cell can also be understood as an intersection of closed half-spaces $H_{\mathbf{v}}^+$ corresponding to $\mathbf{v} \in A_4$ defined as $H_{\mathbf{v}}^+ := \{\mathbf{x} \in \mathcal{S} \ : \ ||\mathbf{x} - \mathbf{v}|| \geq ||\mathbf{v}||\}$. Here, the Voronoi cell $V_{A_4}(\mathbf{0})$ is fully determined by the 20 root vectors, *i.e.* one has

$$V_{A_4}(\mathbf{0}) = \bigcap_{i \neq j} H_{\mathbf{e}_i - \mathbf{e}_j}^+. \tag{5}$$

To obtain a more explicit description of the Voronoi cell $V_{A_4}(\mathbf{0})$, we have to employ the dual lattice A_4^* and its fundamental domain. The dual lattice can be obtained in many ways. Following Conway's approach via glue vectors (Conway & Sloane, 1999), one has

$$A_4^* = \bigcup_{i=0}^{4} [i] + A_4, \tag{6}$$

with the glue vectors

$$[0] = \begin{pmatrix} 0 \\ 0 \\ 0 \\ 0 \\ 0 \end{pmatrix}, \ [1] = \frac{1}{5}\begin{pmatrix} 1 \\ 1 \\ 1 \\ 1 \\ -4 \end{pmatrix}, \ [2] = \frac{1}{5}\begin{pmatrix} 2 \\ 2 \\ 2 \\ -3 \\ -3 \end{pmatrix},$$

$$[3] = \frac{1}{5}\begin{pmatrix} 3 \\ 3 \\ -2 \\ -2 \\ -2 \end{pmatrix}, \ [4] = \frac{1}{5}\begin{pmatrix} 4 \\ -1 \\ -1 \\ -1 \\ -1 \end{pmatrix}. \tag{7}$$

This description allows one immediately to recognize A_4 as a proper sublattice in its dual lattice A_4^*. Moreover, the quotient group $A_4^*/A_4 \simeq C_5$ is of order 5 and the representatives can be chosen as the glue vectors. On the other hand, for upcoming calculations, it is convenient to write down the generators of the lattice. Here, A_4^* is spanned by the vectors

$$\mathbf{a}_i = \mathbf{e}_i - \frac{1}{5}\mathbf{s}, \tag{8}$$

with $1 \leq i \leq 5$ and $\mathbf{s}$ as above. Note that the generating vectors are not linearly independent since $\sum_{i=1}^{5} \mathbf{a}_i = \mathbf{0}$. Finally, one can use them to describe the Voronoi cell,

$$V_{A_4}(\mathbf{0}) = \left\{ \mathbf{x} \in \mathcal{S} \ : \ \mathbf{x} = \frac{1}{2}\sum_{i=1}^{5} \lambda_i \mathbf{a}_i, \ |\lambda_i| \leq 1 \right\}. \tag{9}$$

This object is a regular four-dimensional convex polytope, sometimes considered as a dual polytope to the runcinated 5-cell. It has full symmetry $W(A_4) \times Z_2$. The polytope possesses 30 vertices, 70 bounding edges and 60 bounding polygons (*i.e.* polytopes of dimension two), and 20 bounding polytopes of dimension three. Henceforth, we refer to them as k-boundaries, with $0 \leq k \leq 3$. Baake *et al.* (1990) provided a careful analysis of all k-boundaries and their explicit description, together with one of their corresponding duals in the sense of Kramer & Schlottmann (1989). Important to us here are the 2-boundaries, the vertices and the corresponding dual objects as follows.

The 2-boundary polygons are given by

$$P(+ + - \bigcirc \bigcirc) = \left\{ \frac{1}{2}(\mathbf{a}_1 + \mathbf{a}_2 - \mathbf{a}_3 + \lambda_4\mathbf{a}_4 + \lambda_5\mathbf{a}_5) : |\lambda_i| \leq 1 \right\}, \tag{10}$$

together with all polygons obtained via vertex permutations and sign flips. There is an explicit action of the group H_{A_4} on the set of 2-boundaries. This action can be encoded on the level of the signature $(+ + - \bigcirc \bigcirc)$ as well. In particular, a permutation just permutes the indices, a sign flip affects the signs and $\bigcirc$ remains unchanged. From the geometric point of view, $P(+ + - \bigcirc \bigcirc)$ is a rhombus, and therefore it will play a crucial role in constructing the Penrose rhombus tiling. The 2-boundary dual to $P(+ + - \bigcirc \bigcirc)$ is the triangle $P^*(+ + - \bigcirc \bigcirc)$ defined as

$$P^*(+ + - \bigcirc \bigcirc)$$
$$= \left\{ \mu_1(\mathbf{a}_1 - \mathbf{a}_3) + \mu_2(\mathbf{a}_2 - \mathbf{a}_3) \ : \ \mu_i \geq 0, \mu_1 + \mu_2 \leq 1 \right\}. \tag{11}$$

The correspondence between P and P^* is one to one and the boundaries intersect with their duals at precisely one point.

The 30 vertex points of the Voronoi cell $V_{A_4}(\mathbf{0})$ are exactly those points of $\mathcal{S}$ with the largest distance to the lattice A_4. In terms of the theory of root lattices, they are called holes (Conway & Sloane, 1999). Points with the maximum possible distance to A_4 are called deep holes and the remaining ones are shallow holes. In our case, the vertex

$$P(+ + + + -) = \frac{1}{2}(\mathbf{a}_1 + \mathbf{a}_2 + \mathbf{a}_3 + \mathbf{a}_4 - \mathbf{a}_5)$$
$$= \mathbf{a}_1 + \mathbf{a}_2 + \mathbf{a}_3 + \mathbf{a}_4 \tag{12}$$

and all its images under $W(A_4) \times Z_2$ are the shallow holes, whereas the 20 points of type

$$P(+ + + - -) = \frac{1}{2}(\mathbf{a}_1 + \mathbf{a}_2 + \mathbf{a}_3 - \mathbf{a}_4 - \mathbf{a}_5) = \mathbf{a}_1 + \mathbf{a}_2 + \mathbf{a}_3 \tag{13}$$

are the deep holes.

The dual objects to deep and shallow holes are four-dimensional cells. Namely, one obtains a four-dimensional simplex

$$P^*(+ + + + -) = \left\{ \sum_{i=1}^{4} \mu_i(\mathbf{a}_i - \mathbf{a}_5) \ : \ \mu_i \geq 0, \sum_{i=1}^{4} \mu_i \leq 1 \right\} \tag{14}$$

and a four-dimensional Archimedean polytope

$$P^*(+ + + - -) = \left\{ \sum_{i=1}^{3} \mu_i(\mathbf{a}_i - \mathbf{a}_4) + \sum_{i=1}^{3} \mu_{i+3}(\mathbf{a}_i - \mathbf{a}_5) : \right.$$
$$\mu_i \geq 0, \sum_{i=1}^{3}\mu_i \leq 1, \sum_{i=4}^{6}\mu_i \leq 1,$$
$$\left. \mu_i + \mu_{i+3} \leq 1 \text{ for all } 1 \leq i \leq 3 \right\}, \tag{15}$$

and all their images under the symmetry operations H_{A_4}.

Since A_4 is a lattice, one has the same vertex configuration around any of its points up to translation. Thus, the Voronoi cell $V_{A_4}(\mathbf{v})$ around $\mathbf{v}$ is a translation $V_{A_4}(\mathbf{0}) + \mathbf{v}$. Further, one can collect all k-boundaries and think of them in terms of complexes. In particular, one can define the Voronoi complex

$$\mathcal{V} := \left\{ P \subset \mathcal{S} : P \text{ is a boundary of some } V_{A_4}(\mathbf{v}) \text{ with } \mathbf{v} \in A_4 \right\} \tag{16}$$

and for $0 \leq k \leq 4$ its k-skeleton

$$\mathcal{V}^{(k)} := \left\{ P \in \mathcal{V} \ : \ P \text{ is a } k\text{-boundary} \right\}. \tag{17}$$

The properties of the duality lead to the dual Voronoi complex and its dual k-skeleton as, respectively,

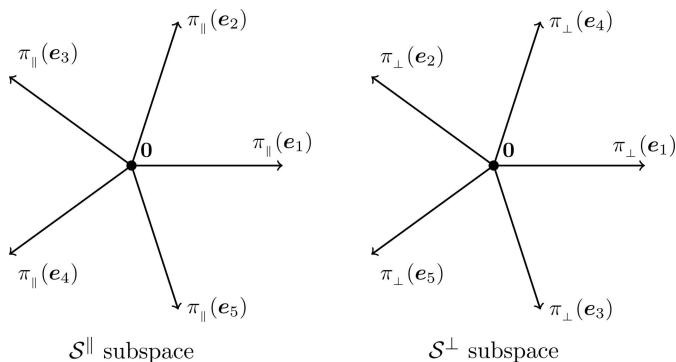$$\mathcal{V}^* := \{ P^* \ : \ P \in \mathcal{V} \}, \tag{18}$$

research papers

Figure 2
Projections of the standard basis $\mathbf{e}_1, \ldots, \mathbf{e}_5$ into the two subspaces $\mathcal{S}^{\parallel}$ and $\mathcal{S}^{\perp}$.

Figure 3
Images of the 2-boundary $P(- + \bigcirc \bigcirc +)$ and its dual $P^*(- + \bigcirc \bigcirc +)$ under the projections $\pi_{\parallel}$ and $\pi_{\perp}$. The solid blue rhombi correspond to projections of the 2-boundary, whereas the dashed line indicates the projection of its dual. The grey points are the 20th roots of unity scaled by $\sqrt{2/5}$.

$$\mathscr{V}^{*(k)} := \{P^* \in \mathscr{V}^* \; : \; P \text{ is a } (4-k)\text{-boundary}\}. \quad (19)$$

Taking any vertex $\mathbf{v}^*$ of the Voronoi cell $V_{A_4}(\mathbf{v})$ for some $\mathbf{v} \in A_4$, i.e. $\mathbf{v}^* \in \mathscr{V}^{(0)}$, the associated dual object, which is a full 4D polytope, will be denoted by $V^*(\mathbf{v}^*)$ as it plays a similar role to the Voronoi cell.

As mentioned above, different points appear within the point sets studied. We have to deal with points of the lattice A_4 and with the vertices of its Voronoi cells. The latter are split into two categories, deep and shallow holes. In order to distinguish them, one can introduce a modulo function r defined for any point $\mathbf{v}^* = \sum_{i=1}^{4} n_i \mathbf{a}_i \in A_4^*$ as

$$r(\mathbf{v}^*) := \left(\sum_{i=1}^{4} n_i \right) \bmod 5. \quad (20)$$

It is clear that $r : A_4^* \to \mathbb{Z}/5\mathbb{Z}$. Since the generating vectors $\mathbf{e}_i - \mathbf{e}_{i+1}$ of the lattice A_4 fulfil

$$\mathbf{e}_i - \mathbf{e}_{i+1} = \mathbf{a}_i - \mathbf{a}_{i+1}, \quad (21)$$

one immediately has

$$A_4 = \ker(r). \quad (22)$$

Further, one obtains the characterization of shallow and deep holes in terms of $r(\mathbf{v}^*)$. In particular,

$$\mathbf{v}^* \text{ is a shallow hole } \Leftrightarrow r(\mathbf{v}^*) = \pm 1 \bmod 5, \quad (23)$$

$$\mathbf{v}^* \text{ is a deep hole } \Leftrightarrow r(\mathbf{v}^*) = \pm 2 \bmod 5. \quad (24)$$

Remark 2.1. The function r corresponds to the index function in de Bruijn's construction (de Bruijn, 1981*a,b*). This is not surprising because de Bruijn's construction implicitly uses the root lattice as a Minkowski embedding of fifth roots of unity, as explained by Baake & Grimm (2013, Section 7.5.2).

3. Representation with fivefold symmetry

We have already mentioned that $W(A_4)$ acts on the generators of A_4 via permutations of the basis vectors $\mathbf{e}_i$. This action has two invariant subspaces, namely $\mathbb{C}\mathbf{s}$ and $\mathcal{S}$. The linear repre-
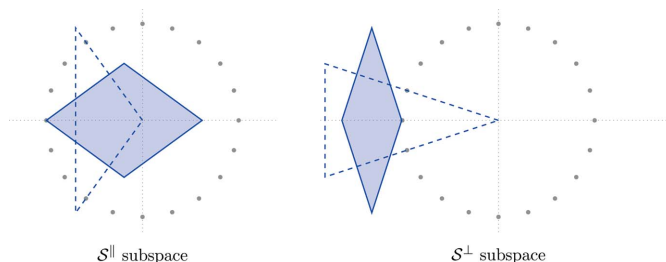
sentation of $S_5 \simeq W(A_4)$ is irreducible on $\mathcal{S}$, and to find a real irreducible representation capturing the fivefold symmetry in plane one has to restrict oneself to a suitable subgroup. Therefore, consider the cyclic group C_5, a subgroup of $W(A_4)$. Its generating element $g = (12345)$ acts on the basis $(\mathbf{e}_1, \ldots, \mathbf{e}_5)$ via the matrix

$$D(g) = \begin{pmatrix} 0 & 0 & 0 & 0 & 1 \\ 1 & 0 & 0 & 0 & 0 \\ 0 & 1 & 0 & 0 & 0 \\ 0 & 0 & 1 & 0 & 0 \\ 0 & 0 & 0 & 1 & 0 \end{pmatrix}. \quad (25)$$

To find the possible representations means to find the real Jordan form of $D(g)$ via an orthogonal matrix J. The real Jordan form reads

$$JD(g)J^{-1} = \begin{pmatrix} \cos\frac{2\pi}{5} & -\sin\frac{2\pi}{5} & 0 & 0 & 0 \\ \sin\frac{2\pi}{5} & \cos\frac{2\pi}{5} & 0 & 0 & 0 \\ 0 & 0 & \cos\frac{4\pi}{5} & -\sin\frac{4\pi}{5} & 0 \\ 0 & 0 & \sin\frac{2\pi}{5} & \cos\frac{2\pi}{5} & 0 \\ 0 & 0 & 0 & 0 & 1 \end{pmatrix}$$

$$= D^{\parallel}(g) \oplus D^{\perp}(g) \oplus D^0(g) \quad (26)$$

and provides three irreducible real representations $D^{\parallel}(g)$, $D^{\perp}(g)$ and $D^0(g)$. The matrix J read columnwise provides a new basis, as one can directly read from

$$JD(g) = \left[D^{\parallel}(g) \oplus D^{\perp}(g) \oplus D^0(g) \right] J. \quad (27)$$

In particular, one has

$$J = \sqrt{\frac{2}{5}} \begin{pmatrix} 1 & \cos\frac{2\pi}{5} & \cos\frac{4\pi}{5} & \cos\frac{4\pi}{5} & \cos\frac{2\pi}{5} \\ 0 & \sin\frac{2\pi}{5} & \sin\frac{4\pi}{5} & -\sin\frac{4\pi}{5} & -\sin\frac{2\pi}{5} \\ 1 & \cos\frac{4\pi}{5} & \cos\frac{2\pi}{5} & \cos\frac{2\pi}{5} & \cos\frac{4\pi}{5} \\ 0 & \sin\frac{4\pi}{5} & -\sin\frac{2\pi}{5} & \sin\frac{2\pi}{5} & -\sin\frac{4\pi}{5} \\ \sqrt{\frac{1}{2}} & \sqrt{\frac{1}{2}} & \sqrt{\frac{1}{2}} & \sqrt{\frac{1}{2}} & \sqrt{\frac{1}{2}} \end{pmatrix}. \quad (28)$$

Since the trivial representation $D^{(0)}(g)$ is carried by the subspace $\mathbb{C}\mathbf{s}$, it follows that $D^{\parallel}(g)$ and $D^{\perp}(g)$ are contained in $\mathcal{S}$. Thus, one has to decompose $\mathcal{S}$ as a direct sum of two subspaces, $\mathcal{S}^{\parallel}$ and $\mathcal{S}^{\perp}$. The representations of g in $\mathcal{S}^{\parallel}$ and $\mathcal{S}^{\perp}$ are rotations about $\frac{2\pi}{5}$ and $\frac{4\pi}{5}$, respectively.

Denote by $\pi_{\parallel}$ and $\pi_{\perp}$ the projections from $\mathcal{S}$ onto $\mathcal{S}^{\parallel}$ and $\mathcal{S}^{\perp}$, respectively. The projections of basis vectors $\pi_{\parallel}(\mathbf{e}_i)$ are given by the first and second rows of the ith column of J, and those of $\pi_{\perp}(\mathbf{e}_i)$ are given by the third and fourth rows of the same column. Fig. 2 depicts the projections of the basis vectors $\mathbf{e}_i$, which exhibit the desired fivefold symmetry. Since $\sum_{i=1}^{5} \pi_{\parallel}(\mathbf{e}_i) = \sum_{i=1}^{5} \pi_{\perp}(\mathbf{e}_i) = \mathbf{0}$, one immediately has $\pi_{\parallel}(\mathbf{a}_i) = \pi_{\parallel}(\mathbf{e}_i)$ and $\pi_{\perp}(\mathbf{a}_i) = \pi_{\perp}(\mathbf{e}_i)$ for all $1 \leq i \leq 5$.

Projecting the 2-boundary P and its dual 2-boundary P^* in both spaces results in a set of triangles and rhombi, which we use later for the construction of the Penrose tiling. Fig. 3 shows the projections of $P(-+\bigcirc\bigcirc+)$ and $P^*(-+\bigcirc\bigcirc+)$. Note that the rhombus vertices always consist of one projection of a shallow hole and three projections of deep holes. The position of the shallow hole will be needed later to distinguish different patterns.

4. Dualization method

One can obtain a space tiling via the *dualization method*. This method was described in detail by Kramer & Schlottmann (1989), and Baake & Grimm (2013) provided an illustrative overview. To employ this method, one needs a Voronoi complex $\mathscr{V}$, its dual (Delone) complex $\mathscr{V}^*$ and a suitable cutting plane, which carries the desired tiling. To obtain a non-periodic tiling, one has to choose the cutting plane so that it contains at most one lattice point.

The construction works in general as follows. Whenever the cutting plane intersects a k-boundary of the Voronoi complex, the dual $(4-k)$-boundary is projected onto the cutting plane.

In our case, we wish to obtain the rhombic Penrose tiling. Therefore, we restrict ourselves to the skeletons $\mathscr{V}^{(2)}$ and $\mathscr{V}^{*(2)}$. Fig. 4 shows the projections of the different (modulo translation) 2-boundaries onto the $\mathcal{S}^{\parallel}$, which are the thick Penrose rhombi.

We choose as the cutting plane a translation of $\mathcal{S}^{\parallel}$ by a vector $\mathbf{c}_{\perp} \in \mathcal{S}^{\perp}$. To ensure aperiodicity, we have to choose $\mathbf{c}_{\perp}$ such that it is not contained in any $\pi_{\perp}$ projection of any 1-boundary of $P^* \in \mathscr{V}^{*(2)}$; see Baake *et al.* (1990) for further details. The vector $\mathbf{c}_{\perp}$ restricts the elements of $\mathscr{V}^{*(2)}$ which one projects onto $\mathcal{S}^{\parallel}$, since the cutting plane $\mathbf{c}_{\perp} + \mathcal{S}^{\parallel}$ intersects a 2-boundary P if and only if $\pi_{\perp}(P^*)$ contains $\mathbf{c}_{\perp}$. The resulting tiling (which depends on the choice of $\mathbf{c}_{\perp}$) can be described as

$$\mathscr{T}_{\mathrm{Pen}}(\mathbf{c}_{\perp}) = \left\{ \pi_{\parallel}(P) \ : \ P \in \mathscr{V}^{(2)}, \ \mathbf{c}_{\perp} \in \pi_{\perp}(P^*) \right\}. \qquad (29)$$

The vertices of $\mathscr{T}_{\mathrm{Pen}}(\mathbf{c}_{\perp})$ are projections of the vertex points of certain Voronoi domains $V(\mathbf{v})$ for some $\mathbf{v} \in A_4$. As already discussed above, these vertices are elements of $A_4^* \backslash A_4$ and are of four translation types, as characterized by the function r. The vertex points $\mathbf{v}^*$ are split into four orbits with respect to the translation action of A_4. For each orbit, one can choose a representative $\mathbf{v}_i^*$, for example

$$\mathbf{v}_1^* := \mathbf{a}_1, \quad \mathbf{v}_2^* := \mathbf{a}_1 + \mathbf{a}_3, \quad \mathbf{v}_3^* := -\mathbf{a}_1 - \mathbf{a}_3, \quad \mathbf{v}_4^* := -\mathbf{a}_1. \qquad (30)$$

From the construction of $\mathscr{T}_{\mathrm{Pen}}(\mathbf{c}_{\perp})$, we see that a point $\mathbf{v}^* \in A_4^* \backslash A_4$ is a pre-image of a vertex point in $\mathscr{T}_{\mathrm{Pen}}(\mathbf{c}_{\perp})$ if and only if $\mathbf{v}^* \in P$ with $\mathbf{c}_{\perp} \in \pi_{\perp}(P^*)$ for some $P \in \mathscr{V}^{(2)}$. Note that if a point is an element of a k-boundary, the dual $(4-k)$-
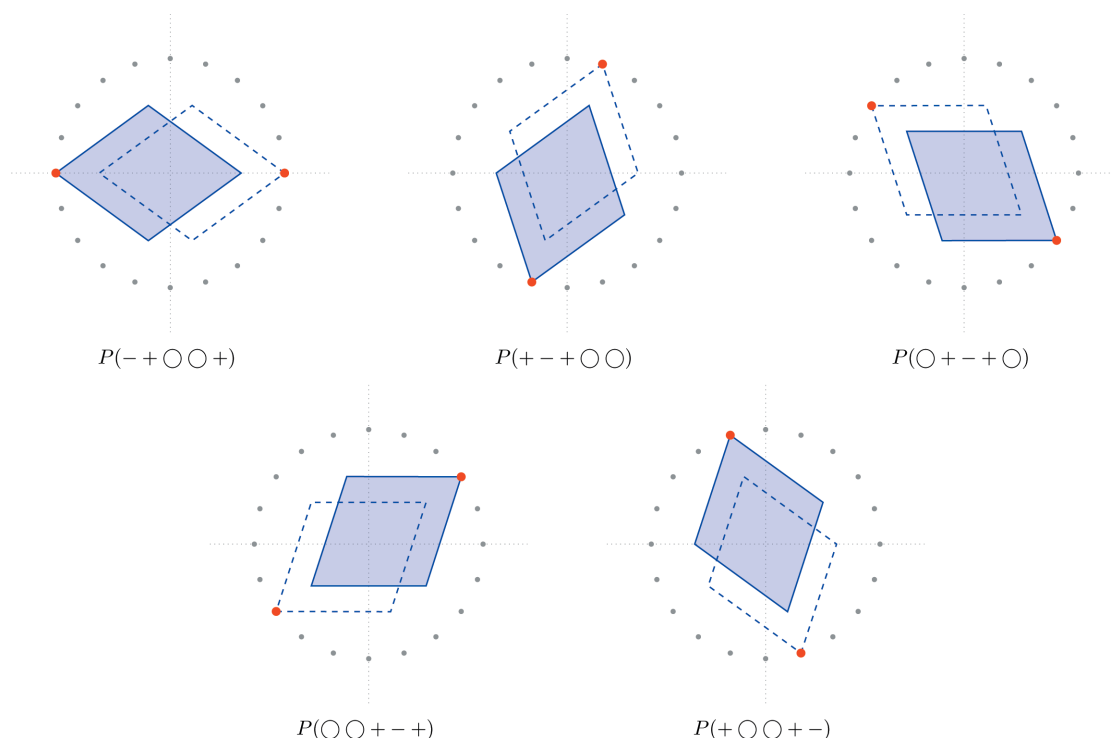

$$P(-+\bigcirc\bigcirc+) \qquad P(+-+\bigcirc\bigcirc) \qquad P(\bigcirc+-+\bigcirc)$$

$$P(\bigcirc\bigcirc+-+) \qquad P(+\bigcirc\bigcirc+-)$$

Figure 4
Projections of the different (modulo translation) 2-boundaries P in $\mathcal{S}^{\parallel}$ which result in a thick rhombus. The solid rhombi correspond to the labels, whereas the dashed rhombi are their space inversions. The red point attached to a given rhombus indicates the shallow hole. The grey points are the 20th roots of unity scaled by a factor $\sqrt{2/5}$.
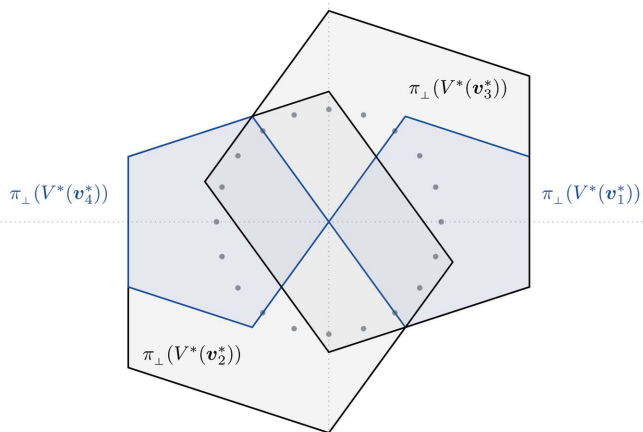
Figure 5
Projections $\pi_\perp(V^*(\mathbf{v}_i^*)) \subset \mathcal{S}^\perp$ corresponding to the windows. The blue pentagons carry the $\pi_\perp$-projections of shallow holes, whereas the black ones comprise the projections of deep holes. Note that for every window there exists its own lattice. Thus, even though there is a non-trivial intersection of windows, the resulting points must differ, as one expects. The grey points are the 20th roots of unity scaled by a factor $\sqrt{2/5}$.

boundary lies in the dual cell of that point and vice versa. So $\mathbf{v}^* \in P$ if and only if $P^* \subset V^*(\mathbf{v}^*)$, with $V^*(\mathbf{v}^*)$ being a translation of a dual four-dimensional cell of the form (14) or (15). Thus, $\pi_\|(\mathbf{v}^*)$ is a vertex in $\mathcal{T}_{\mathrm{Pen}}(\mathbf{c}_\perp)$ if and only if $\mathbf{c}_\perp \in \pi_\perp(V^*(\mathbf{v}^*))$. Two points $\mathbf{v}_1^*$ and $\mathbf{v}_2^*$ with $r(\mathbf{v}_1^*) = r(\mathbf{v}_2^*)$ can only differ by a lattice vector. The choice of representatives (30) allows us to relate any point $\mathbf{v}^*$ with one of them. Define $q(\mathbf{v}^*) := \mathbf{v}^* - \mathbf{v}_{r(\mathbf{v}^*)}^* \in A_4$ for any $\mathbf{v}^*$. Since

$$V^*(\mathbf{v}^*) = V^*(\mathbf{v}^* - \mathbf{v}_{r(\mathbf{v}^*)}^* + \mathbf{v}_{r(\mathbf{v}^*)}^*) = q(\mathbf{v}^*) + V^*(\mathbf{v}_{r(\mathbf{v}^*)}^*), \quad (31)$$

one has

$$\mathbf{c}_\perp \in \pi_\perp(V^*(\mathbf{v}^*)) \Longleftrightarrow \mathbf{c}_\perp - \pi_\perp(q(\mathbf{v}^*)) \in \pi_\perp\big(V^*(\mathbf{v}_{r(\mathbf{v}^*)}^*)\big). \quad (32)$$

This allows us to rewrite the set of vertex points of $\mathcal{T}_{\mathrm{Pen}}(\mathbf{c}_\perp)$ as

$$\big\{\pi_\|(\mathbf{v}^*) \; : \; \mathbf{v}^* \in A_4^*\backslash A_4, \; \mathbf{c}_\perp - \pi_\perp(q(\mathbf{v}^*)) \in \pi_\perp\big(V^*(\mathbf{v}_{r(\mathbf{v}^*)}^*)\big)\big\}. \quad (33)$$

This description shows that the set of vertices can be understood as four cut-and-project sets with lattices $\mathbf{v}_i^* + A_4 \subset \mathcal{S}$ and windows $\pi_\perp(V^*(\mathbf{v}_i^*)) \subset \mathcal{S}^\perp$, $1 \leq i \leq 4$. Fig. 5 shows all four windows $\pi_\perp(V^*(\mathbf{v}_i^*))$ in $\mathcal{S}^\perp$; for more detail see Example 7.11 and Remark 7.8 in Baake & Grimm (2013).

Once we have established the description of all vertices of $\mathcal{T}_{\mathrm{Pen}}(\mathbf{c}_\perp)$, we can further determine a *vertex configuration* of each vertex, *i.e.* all tiles in $\mathcal{T}_{\mathrm{Pen}}(\mathbf{c}_\perp)$ surrounding the vertex $\pi_\|(\mathbf{v}^*)$. The description (29) provides us with a characterization of the tiles surrounding $\pi_\|(\mathbf{v}^*)$. Indeed, a tile $\pi_\|(P)$ belongs to a vertex configuration of $\pi_\|(\mathbf{v}^*)$ if and only if $P \in \mathcal{V}^{(2)}$, $\mathbf{v}^* \in P$ and $\mathbf{c}_\perp \in \pi_\perp(P^*)$. The problem of finding a vertex configuration around an arbitrary vertex point can be reduced using translation symmetry. We can restrict ourselves to finding all vertex configurations around a representative of each translation class, *i.e.* around the points $\mathbf{v}_i^*$. We can then rewrite the conditions above as $P^* - q(\mathbf{v}^*) \subset V^*(\mathbf{v}_{r(\mathbf{v}^*)}^*)$ and $\mathbf{c}_\perp - \pi_\perp(q(\mathbf{v}^*)) \in \pi_\perp(P^*) - \pi_\perp(q(\mathbf{v}^*))$. So P belongs to a
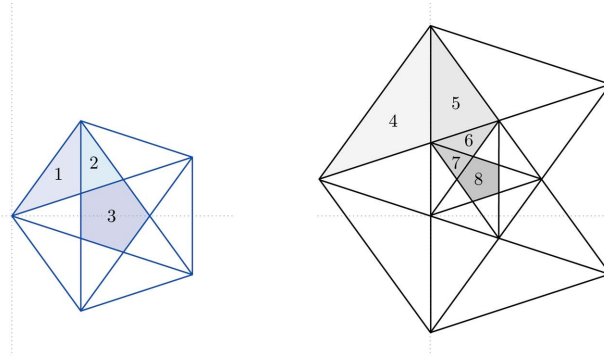

Figure 6
Subdivision of $\pi_\perp(V^*(\mathbf{v}_1^*))$ (blue) and $\pi_\perp(V^*(\mathbf{v}_3^*))$ (black) into elementary polygons. The eight possible vertex configurations (modulo rotation by $2\pi/5$ and space inversion) correspond to eight distinct elementary polygons.

vertex configuration of a point $\mathbf{v}^*$ if and only if the translation of its dual P^* by $q(\mathbf{v}^*)$ is a 2-boundary of the dual cell $V^*(\mathbf{v}_{r(\mathbf{v}^*)}^*)$. This gives an algorithm for obtaining the complete vertex configuration around the vertex $\pi_\|(\mathbf{v}^*)$ as follows.

(1) Find all $\mathbf{w}^* \in A_4^*\backslash A_4$ such that $\mathbf{c}_\perp - \pi_\perp(q(\mathbf{w}^*)) \in \pi_\perp(V^*(\mathbf{v}_{r(\mathbf{v}^*)}^*))$.

(2) For all $\mathbf{w}^*$ found in Step (1), take the 2-boundary P^* of the dual cell $V^*(\mathbf{v}_{r(\mathbf{v}^*)}^*)$ with $\mathbf{c}_\perp - \pi_\perp(q(\mathbf{w}^*)) \in \pi_\perp(P^*)$. Then, $\pi_\|(\mathbf{w}^*) + \pi_\|(P)$ is a tile around $\pi_\|(\mathbf{v}^*)$.

We choose $\mathbf{c}_\perp$ so that $\mathbf{c}_\perp - \pi_\perp(q(\mathbf{w}^*))$ lies in the interior of $\pi_\perp(P^*)$. This is a crucial observation. It forces all tiles $\pi_\|(\mathbf{w}^*) + \pi_\|(P)$ belonging to a particular vertex configuration to have, at the level of $\pi_\perp(P^*)$, an overlap in the $\pi_\perp(V^*(\mathbf{v}_{r(\mathbf{v}^*)}^*))$. We can use this property to determine and characterize all possible vertex configurations with respect to translations in $\mathcal{S}^\perp$ as follows: a set $\mathcal{W} \subset \mathcal{V}^{(2)}$ of 2-boundaries is a valid vertex configuration of a vertex of type i if and only if $\mathcal{W}$ is maximal with respect to the property that $\cap_{P \in \mathcal{W}} \pi_\perp(P^*)$ is non-empty. The projection of 2-boundaries of the dual cells $V^*(\mathbf{v}_i^*)$ divides the $\pi_\perp(V^*(\mathbf{v}_i^*))$ into convex polygons, called *elementary polygons* (Baake *et al.*, 1990). They have pairwise distinct interiors, each representing a distinct vertex configuration (and vice versa). Fig. 6 shows the elementary polygons for $\pi_\perp(V^*(\mathbf{v}_1^*))$ and $\pi_\perp(V^*(\mathbf{v}_3^*))$. The corresponding vertex configurations are shown in Fig. 7.
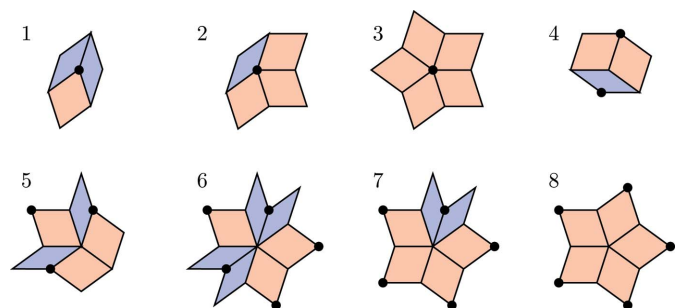

Figure 7
All possible vertex configurations (up to rotation by $2\pi/5$ and space inversion) which are in one-to-one correspondence with the elementary polygons in Fig. 6. The black points indicate the positions of shallow holes.

The choice of the cutting plane ensures that the projections of the vertices of a valid infinite Penrose tiling onto $\mathcal{S}^{\perp}$ are dense and uniformly distributed. Thus, we can use them to determine the frequencies of the vertex configurations via the areas of the elementary polygons. Denote by E an elementary polygon. The relative frequency $\nu_{\mathscr{C}(E)}$ of vertex configuration $\mathscr{C}(E)$ corresponding to the elementary polygon E is then given by

$$\nu_{\mathscr{C}(E)} = \frac{\text{Area}(E)}{\sum_{i=1}^{4} \text{Area}(\pi_{\perp}(V^{*}(\mathbf{v}_{i}^{*})))} = \frac{\text{Area}(E)}{\sqrt{5(5 + 2\sqrt{5})}}, \quad (34)$$

i.e. by exactly the fraction of the total area of windows it occupies. We list the frequencies of all vertex configurations in Table 1. We include the frequency of the given patch as well as the cumulative frequency of all patches of the same type, *i.e.* all patches that lie in the same orbit under the rotation and space inversion.

The sum of all total frequencies equals one, and thus we have a consistency check. Since Penrose tiling defines a strictly ergodic dynamic system (in the usual way) (Robinson, 1996), we conclude that there are no other vertex configurations. If there were any others, they would come with a strictly positive measure, which is the patch frequency.

Recall that the *frequency module* of a tiling space $\mathbb{X}$ (in our case, the tiling space generated by rhombic Penrose tilings) is the minimal $\mathbb{Z}$-module $\mathcal{M}_{\mathbb{X}}$ that contains all frequencies of finite patches of the tiling. Here, we obtain the following specific result.

Proposition 4.1. The frequency module $\mathcal{M}_{\mathscr{T}_{\text{Pen}}}$ of the Penrose tiling is

$$\mathcal{M}_{\mathscr{T}_{\text{Pen}}} = \frac{1}{10}\mathbb{Z}[\tau]. \quad (35)$$

Proof. Consider any patch of the Penrose tiling. We can always find an $n \in \mathbb{N}$ such that this given patch is contained in a level-n supertile of some vertex configuration $\mathscr{C}$. Since the Penrose tiling is an inflation/deflation tiling, its level-n supertiles around a given vertex configuration are equivalent to the original vertex configuration scaled by a factor τ^{n}. Therefore, the supertile itself has a frequency given by $(1/\tau^{2n}) \cdot \nu_{\mathscr{C}}$. The factor $(1/\tau^{2n})$ comes from the observation that the frequency is inversely proportional to the area. Since τ is a unit in $\mathbb{Z}[\tau]$, so is τ^{2n}. Thus, to determine the frequency module, it suffices to consider the $\mathbb{Z}$-module generated by $\nu_{\mathscr{C}(E)_i}$, $1 \leq i \leq 8$, *i.e.*

$$\mathcal{M}_{\mathscr{T}_{\text{Pen}}} = \langle \nu_{\mathscr{C}(E_i)} : 1 \leq i \leq 8 \rangle_{\mathbb{Z}}. \quad (36)$$

Since $\nu_{\mathscr{C}(E_1)} + 2\nu_{\mathscr{C}(E_5)} + \nu_{\mathscr{C}(E_4)} = 1/10$ and $\nu_{\mathscr{C}(E_4)} + \nu_{\mathscr{C}(E_5)} = (\tau - 1)/10$, one has

$$\mathcal{M}_{\mathscr{T}_{\text{Pen}}} = \langle \nu_{\mathscr{C}(E_i)} : 1 \leq i \leq 8 \rangle_{\mathbb{Z}} = \frac{1}{10}\langle 1, \tau \rangle_{\mathbb{Z}} = \frac{1}{10}\mathbb{Z}[\tau]. \quad (37)$$

□

Table 1
Frequencies of vertex configurations in Penrose tilings, all belonging to $\mathbb{Q}(\tau)$ with τ being the golden ratio.

The second column shows the frequencies of particular patches, those in Fig. 7. The last column gives the total frequencies of a patch of a given type, *i.e.* a patch and all its images under the allowed rotations and space inversion.

Vertex configuration	Frequency $\nu_{\mathscr{C}(E_i)}$	Total frequency ν_i
1	$\frac{1}{10}(5 - 3\tau)$	$5 - 3\tau = \tau^{-4}$
2	$\frac{1}{10}(5\tau - 8)$	$5\tau - 8 = \tau^{-5}$
3	$\frac{1}{10}(18 - 11\tau)$	$\frac{1}{5}(18 - 11\tau) = \frac{2\tau - 1}{5}\tau^{-5}$
4	$\frac{1}{10}(2 - \tau)$	$2 - \tau = \tau^{-2}$
5	$\frac{1}{10}(2\tau - 3)$	$2\tau - 3 = \tau^{-3}$
6	$\frac{1}{10}(13 - 8\tau)$	$13 - 8\tau = \tau^{-6}$
7	$\frac{1}{10}(13\tau - 21)$	$13\tau - 21 = \tau^{-7}$
8	$\frac{1}{10}(47 - 29\tau)$	$\frac{1}{5}(47 - 29\tau) = \frac{2\tau - 1}{5}\tau^{-7}$

5. General patch frequencies and their calculation

The idea behind the above construction can be extended to any patch in Penrose rhombic tilings. Choose a vertex of a tile and relate all tiles of the patch to this vertex. One has to be careful and distinguish consistently between deep and shallow holes. One then obtains a list of all tiles and their relative positions with respect to the chosen central tile. By transitioning into $\mathcal{S}^{\perp}$, one obtains a list of all dual triangles and their relative distance. Their intersection determines the frequency of the patch in the same way as in the case of vertex configuration. This intersection is always a convex polygon (since one intersects a finite number of triangles) and its area can be computed easily. Note that some minimal subset of the triangles entirely determines this intersection and working only with them can increase the computational speed considerably.

Let us list, in Fig. 8, all possible tiles together with the shallow holes attached to each of them. We place them so that the shallow hole indicates the 'origin' relative to the given tile. More precisely, we depict them in coordinates which are translated by the shallow vertex of a given tile. We also include the dual tile and its projection in $\mathcal{S}^{\perp}$. The projection is also centred on the relative origin. There is an extra advantage to such a choice, namely, the vertices of dual triangles in $\mathcal{S}^{\perp}$ are placed at the 20th roots of unity scaled by the factor $\sqrt{2/5}$. Since the frequency is given by a ratio of two areas, the scaling factor does not play a role. This allows a precise calculation, simply by employing a suitable subfield of $\mathbb{Q}[\exp(\pi i/10)]$. In fact, one can work with integer coefficients.

We can now describe the algorithm that allows us to determine the frequency of a given patch. We start with an arbitrary finite patch of the Penrose tiling.

(1) Detect all shallow holes in the patch. This can be done via the allowed vertex configurations.

(2) Identify the type of each tile in the patch as R_i, S_i or their space inversions (RI_i, SI_i) from the list given in Fig. 8.

(3) Choose any shallow hole, the 'origin', from the vertices of the patch and fix it.

(4) Make a list of all positions of all tiles (their shallow holes) relative to the origin. Since the edges of the rhombi are projections $\pi_\parallel(\mathbf{a}_i)$, the resulting position vector can always be written as $\sum_{i\in\mathcal{I}} \epsilon_i \pi_\parallel(\mathbf{a}_i)$, where $\mathcal{I}$ parametrizes the path on the edges from the origin to the desired point and $\epsilon_i \in \{\pm 1\}$ denotes the orientation of the vectors $\pi_\parallel(\mathbf{a}_i)$ in the path.

(5) Apply the dual correspondence, *i.e.* to each translated tile $T + \sum_{i\in\mathcal{I}} \epsilon_i \pi_\parallel(\mathbf{a}_i)$ assign the dual $T^* + \sum_{i\in\mathcal{I}} \epsilon_i \pi_\perp(\mathbf{a}_i)$, with $T \in \{R_i, S_i, RI_i, SI_i\}$.

(6) Find an intersection of all $T^* + \sum_{i\in\mathcal{I}} \epsilon_i \pi_\perp(\mathbf{a}_i)$ from the list. This can be done via any clipping algorithm, for example the Sutherland–Hodgman algorithm (Sutherland & Hodgman, 1974).

(7) Calculate the area of the intersection.

(8) Divide the area of the intersection by the total area of the windows, *i.e.* by $\sqrt{5(5+2\sqrt{5})}$. This yields the relative frequency.

Note that one can choose any clipping algorithm since one has to deal with triangles only (for different lattices one obtains general convex polygons). Under this condition, most
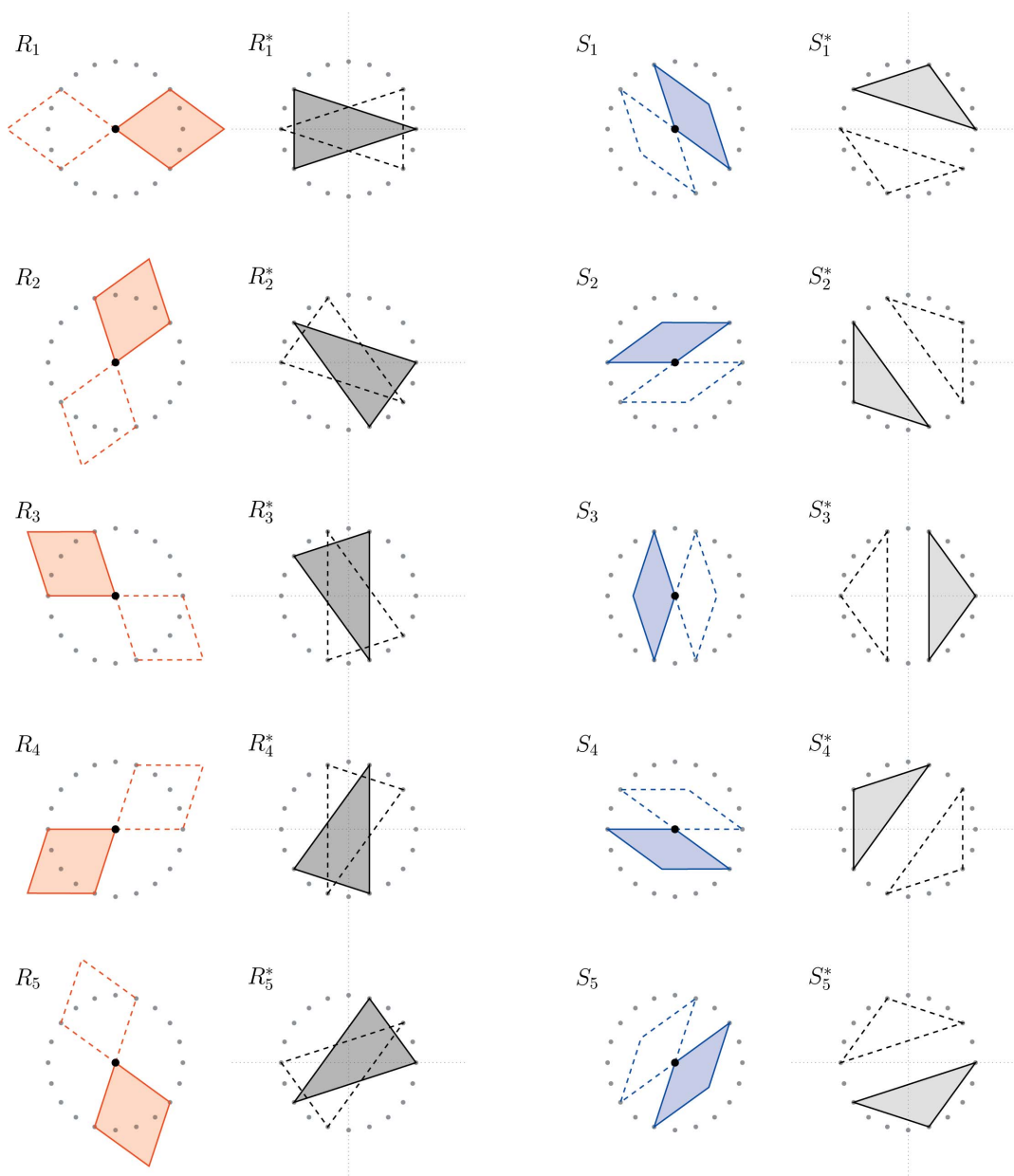
Figure 8
A list of all possible tiles (with respect to their orientations and placement of a shallow hole) in rhombic Penrose tilings and their duals in $\mathcal{S}^\perp$. Tiles are depicted relative to the shallow hole. The exact correspondence between a tile in the list and a projection of a 2-boundary is, for example, the following. If a tile of type R_1 corresponds to $\pi_\parallel(P(- + \bigcirc\bigcirc +))$, the dual triangle R_1^* *is equal to* $\pi_\perp(P^*(- + \bigcirc\bigcirc +)) + \pi_\perp(\mathbf{a}_1)$, *i.e.* we capture its actual position in $\perp$-space. Fixing the positions of the duals allows us to work in coordinates relative to a given point, the 'origin'. Everything is then shifted by a suitable vector representing the relative distances of objects from the origin.
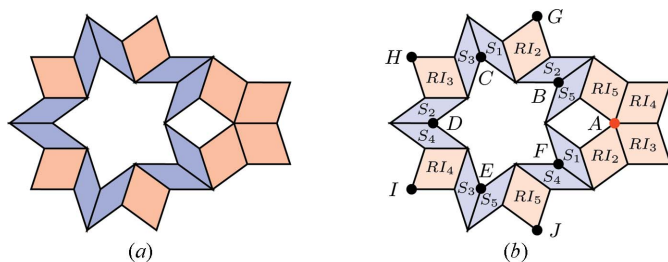
Figure 9
(*a*) The original plain diamond ring patch with 18 tiles. (*b*) The same patch after the identification process with indicated shallow holes (dots) and with a chosen origin (red dot). The tiles are labelled with respect to the shallow hole they contain and the picture shows the situation after Step 3 of the algorithm.

Table 2
The positions of shallow holes of the diamond ring patch relative to the origin A; in particular, this is the result of Step 4 of the algorithm.

For better readability, we abbreviate $\pi_\perp(\mathbf{a}_i)$ to $\mathbf{a}_i^\perp$.

Shallow hole	Translation vector
B	$\mathbf{a}_2^\perp + \mathbf{a}_3^\perp + \mathbf{a}_4^\perp$
C	$-\mathbf{a}_1^\perp + \mathbf{a}_2^\perp + 2\mathbf{a}_3^\perp + \mathbf{a}_4^\perp$
D	$-\mathbf{a}_1^\perp + 2\mathbf{a}_3^\perp + 2\mathbf{a}_4^\perp$
E	$-\mathbf{a}_1^\perp + \mathbf{a}_3^\perp + 2\mathbf{a}_4^\perp + \mathbf{a}_5^\perp$
F	$\mathbf{a}_3^\perp + \mathbf{a}_4^\perp + \mathbf{a}_5^\perp$
G	$-\mathbf{a}_1^\perp + \mathbf{a}_2^\perp + \mathbf{a}_3^\perp - \mathbf{a}_5^\perp$
H	$-2\mathbf{a}_1^\perp + 2\mathbf{a}_3^\perp + \mathbf{a}_4^\perp - \mathbf{a}_5^\perp$
I	$-2\mathbf{a}_1^\perp - \mathbf{a}_2^\perp + \mathbf{a}_3^\perp + 2\mathbf{a}_4^\perp$
J	$-\mathbf{a}_1^\perp - \mathbf{a}_2^\perp + \mathbf{a}_4^\perp + \mathbf{a}_5^\perp$

clipping algorithms are sufficiently robust. Moreover, at least the Sutherland–Hodgman algorithm ensures that the resulting coordinates of the vertices of the intersection are contained in the same field as the coordinates of the polygons, since each step of the algorithm relies on solving systems of two linear equations with the coefficients being the coordinates of the vertices of the polygons.

Finally, computing the area of a polygon determined by its vertices can be done via the shoelace formula (or Gauss's area formula) (Koecher & Krieg, 2007), which is also within the field.

Let us demonstrate the procedure on the following patch [this patch, called a *diamond ring*, supports an eigenfunction of a discrete Laplacian on the Penrose tiling; see Damanik *et al.* (2022) for further details]. Fig. 9(*a*) shows the initial data of the algorithm. Fig. 9(*b*) shows the results of Step 2 (determining the shallow holes) and Step 3 (labelling the tiles). Table 2 summarizes the paths from the origin (red point A) to the (black) shallow holes (labelled with letters B to J), *i.e.* the relative translation vectors, *i.e.* the result of Step 4. Finally,

Fig. 10 shows the result of the correspondence described in Step 5, *i.e.* it depicts the corresponding dual triangles in $\mathcal{S}^\parallel$ and their intersection (Step 6), which is, in this particular case, a triangle. Its area (Step 7) is $1/\sqrt{2(1165 + 521\sqrt{5})}$. Thus, the frequency of the diamond ring patch reads $\nu_{\mathrm{diam}} = \frac{1}{10}(34 - 21\tau)$ $= \frac{1}{10}\tau^{-8} \in \mathcal{M}_{\mathcal{T}_{\mathrm{Pen}}}$. The total frequency of this patch (*i.e.* of all its possible rotations and space inversions) is $\nu_{\mathrm{diam}}^{\mathrm{tot}} = 34 - 21\tau$. We include other patches mentioned by Damanik *et al.* (2022) in Appendix A.

The algorithm for obtaining patch frequencies can also be used for an entire class of tilings, namely, for those tilings obtained via the dualization method. Usually, there is no need to distinguish between deep and shallow holes, which makes the procedure slightly easier. On the other hand, another restriction may occur, but the idea and the basic scheme remain the same. By interchanging the roles of triangles and rhombi, one can obtain the Tübingen Triangle Tiling (TTT) (Baake *et al.*, 1990). Using a different root lattice, one can also obtain patch frequencies for a plethora of quasiperiodic tilings with eight- and 12-fold symmetry, including the Ammann–Beenker tiling (Baake & Joseph, 1990; Baake *et al.*, 1991). Further details are given in Appendix B.
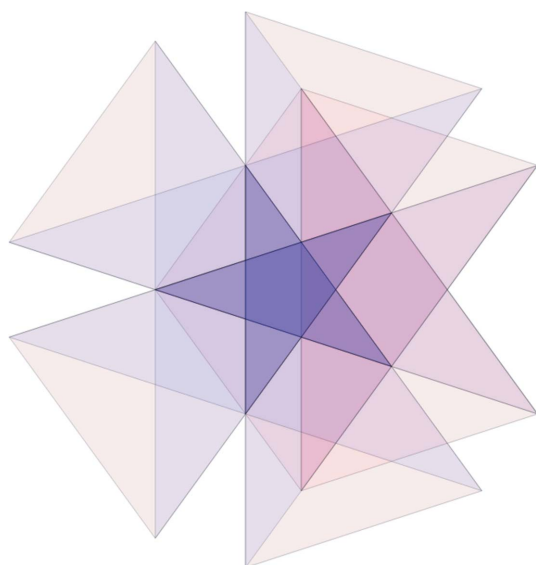
APPENDIX A
Exact results for patches in Penrose tilings

In Figs. 11 to 17, we depict other patches that appear in Damanik *et al.* (2022) and the corresponding dual triangles in $\mathcal{S}^\perp$. We also give the frequencies of these patches.

APPENDIX B
Ammann–Beenker tiling

Here, we briefly describe the setting for the Ammann–Beenker octagonal tiling. This tiling can be obtained via the dualization of the four-dimensional cubic lattice $\mathbb{Z}^4 = \langle \mathbf{e}_1, \mathbf{e}_2, \mathbf{e}_3, \mathbf{e}_4 \rangle_{\mathbb{Z}}$ which is self-dual. Recall that the Voronoi cell around the origin is the 4-cube given as

$$V_{\mathbb{Z}^4}(\mathbf{0}) = \left\{ \mathbf{x} \in \mathbb{R}^4 \; : \; |\mathbf{x}_i| \leq \frac{1}{2} \text{ for all } 1 \leq i \leq 4 \right\}. \quad (38)$$

Figure 10
The intersection of dual tiles of the diamond ring patch. They possess a common intersection, the small violet triangle.
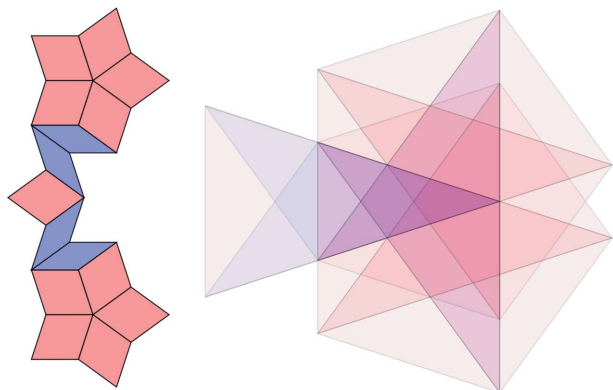
Figure 11
The two star patch with 15 tiles. Its frequency is $\nu_{\text{two}} = \frac{1}{5}(34 - 21\tau) = \frac{1}{5}\tau^{-8}$.
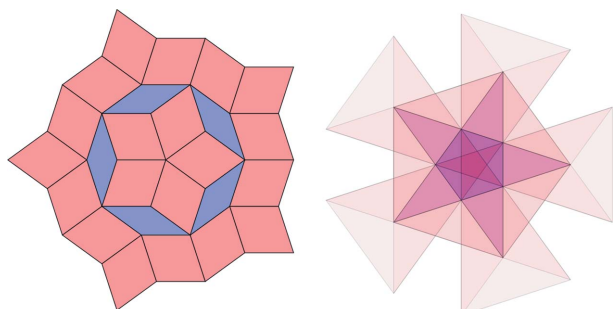

Figure 12
The filled circle patch with 25 tiles. Its frequency is $\nu_{\text{filled}} = \frac{1}{10}(123 - 76\tau) = \frac{2\tau - 1}{10}\tau^{-9}$.
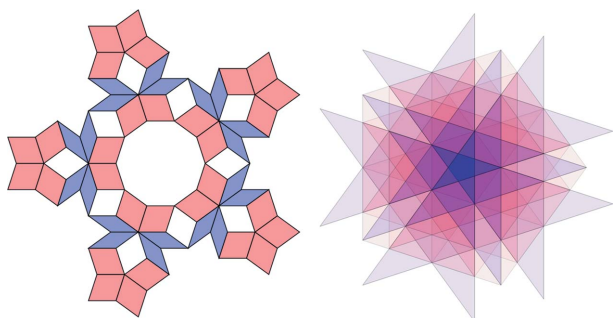

Figure 13
The big star patch with 50 tiles. Its frequency is $\nu_{\text{big}} = \frac{1}{10}(123 - 76\tau) = \frac{2\tau - 1}{10}\tau^{-9}$.

The dual cells of the corresponding Voronoi complex are of the form

$$V^*_{\mathbb{Z}^4}(\mathbf{0}^*) = a, \left\{\mathbf{x} \in \mathbb{R}^4 \; : \; 0 \le \mathbf{x}_i \le 1 \text{ for all } 1 \le i \le 4\right\}$$

$$= V_{\mathbb{Z}^4}(\mathbf{0}) + \frac{1}{2}(1, 1, 1, 1)^{\text{T}}. \qquad (39)$$

The symmetry group of the Voronoi cell is the *hyper-octahedral group* $\Omega(4)$ (Baake *et al.*, 1982). All 2-boundaries of $V_{\mathbb{Z}^4}(\mathbf{0})$ are squares of the form

$$Q(++\bigcirc\bigcirc) = \frac{1}{2}\{\mathbf{e}_1 + \mathbf{e}_2 + \lambda_1\mathbf{e}_3 + \lambda_2\mathbf{e}_4 \; : \; -1 \le \lambda_1, \lambda_2 \le 1\}, \qquad (40)$$

and all its possible images under the action of $\Omega(4)$, which acts via permutations and sign flips. Altogether we obtain 24
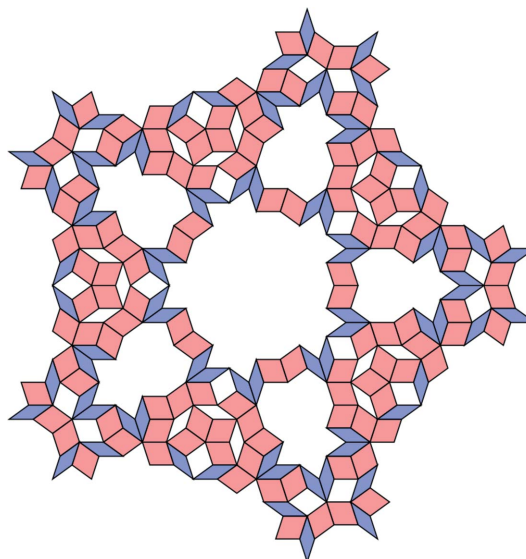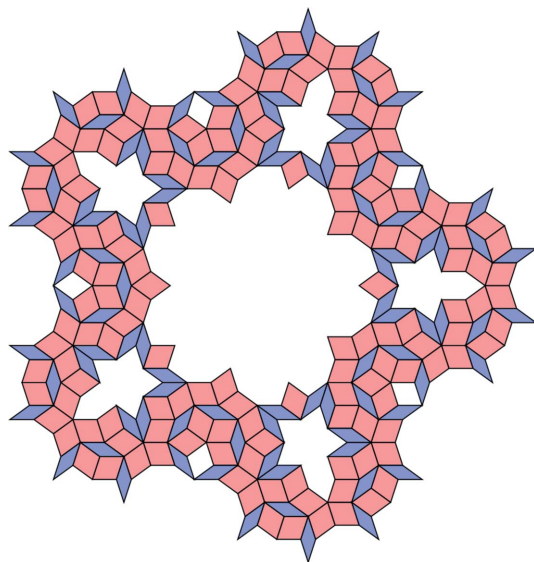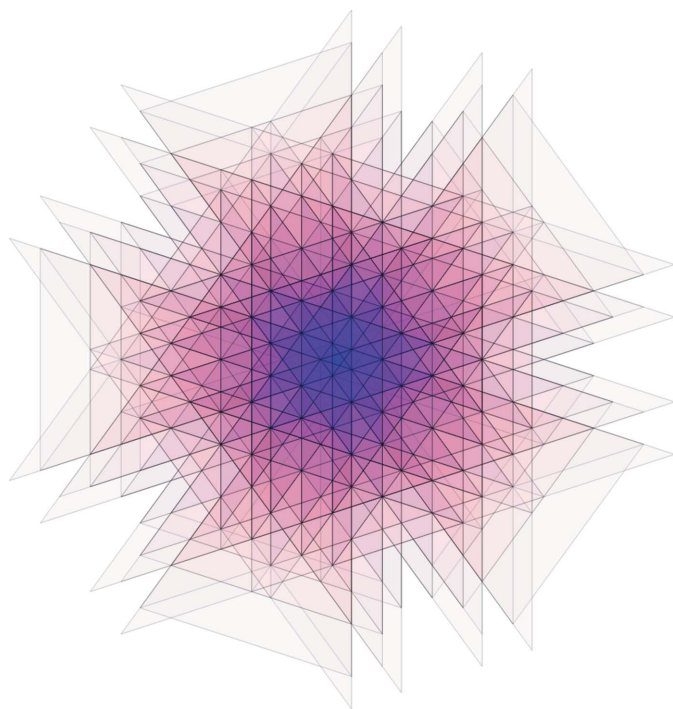

Figure 14
A 200-tile patch.
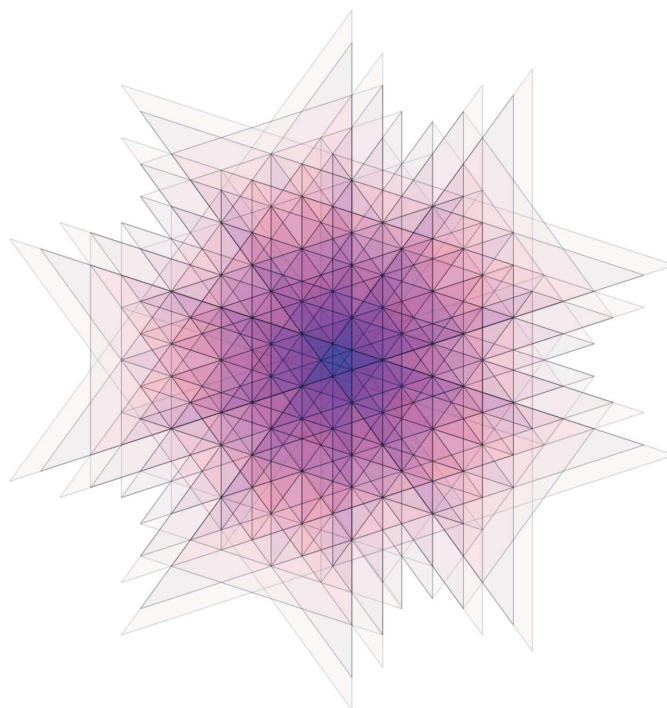
Figure 15
The dual image of the patch from Fig. 14. The frequency of this patch is $\nu_{\text{huge1}} = \frac{1}{10}(2207 - 1364\tau) = \frac{2\tau - 1}{10}\tau^{-15}$.

congruent 2-boundaries. The dual boundaries are squares as well,

$$Q^*(++\bigcirc\bigcirc) = \{\mu_1\mathbf{e}_1 + \mu_2\mathbf{e}_2 \; : \; 0 \le \mu_1, \mu_2 \le 1\}, \qquad (41)$$

and the pairing of boundaries Q and their dual boundaries Q^* is one to one.

As in the case of the Penrose tiling, we need to find a suitable subgroup of the holohedry $\Omega(4)$ which possesses an (irreducible) representation in a plane. One can consider the dihedral group D_8 which is a proper subgroup of $\Omega(4)$. This subgroup is generated by two elements g_8, s satisfying

Figure 16
A 245-tile patch.

Figure 17
The dual image of the patch from Fig. 16. The frequency of this patch is $\nu_{\text{huge2}} = \frac{1}{10}(2207 - 1364\tau) = \frac{2\tau-1}{10}\tau^{-15}$.

$g_8^8 = s^2 = e$ and $(g_8 s)^2 = e$. The generators act on the basis vectors $\mathbf{e}_i$ via the matrices

$$D(g_8) = \begin{pmatrix} 0 & 0 & 0 & -1 \\ 1 & 0 & 0 & 0 \\ 0 & 1 & 0 & 0 \\ 0 & 0 & 1 & 0 \end{pmatrix}, \quad D(s) = \begin{pmatrix} 1 & 0 & 0 & 0 \\ 0 & 0 & 0 & -1 \\ 0 & 0 & -1 & 0 \\ 0 & -1 & 0 & 0 \end{pmatrix}.$$

$$(42)$$

These matrices can be simultaneously brought to the real Jordan form, namely
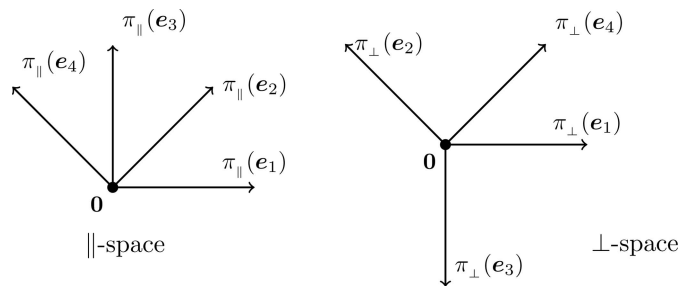
Figure 18
Projections of the standard basis $\mathbf{e}_1, \ldots, \mathbf{e}_4$ onto the two subspaces.

$$D(g_8) \simeq \begin{pmatrix} \cos\frac{\pi}{4} & -\sin\frac{\pi}{4} & 0 & 0 \\ \sin\frac{\pi}{4} & \cos\frac{\pi}{4} & 0 & 0 \\ 0 & 0 & \cos\frac{3\pi}{4} & -\sin\frac{3\pi}{4} \\ 0 & 0 & \sin\frac{3\pi}{4} & \cos\frac{3\pi}{4} \end{pmatrix},$$

$$D(s) \simeq \begin{pmatrix} 1 & 0 & 0 & 0 \\ 0 & -1 & 0 & 0 \\ 0 & 0 & 1 & 0 \\ 0 & 0 & 0 & -1 \end{pmatrix},$$

$$(43)$$

using the matrix

$$J = \sqrt{\frac{1}{2}}\begin{pmatrix} 1 & \sqrt{\frac{1}{2}} & 0 & -\sqrt{\frac{1}{2}} \\ 0 & \sqrt{\frac{1}{2}} & 1 & \sqrt{\frac{1}{2}} \\ 1 & -\sqrt{\frac{1}{2}} & 0 & \sqrt{\frac{1}{2}} \\ 0 & \sqrt{\frac{1}{2}} & -1 & \sqrt{\frac{1}{2}} \end{pmatrix}.$$

$$(44)$$

Taking the first two entries of each column of J, one gains the projections of the basis vectors into the $\parallel$-space, whereas taking the third and fourth ones gives their $\perp$-projection. The projections are shown in Fig. 18 and they already reveal the two shapes of tiles, namely a square, and a rhombus with acute angle $\frac{\pi}{4}$.

The projections of the basis exhibit the desired octagonal symmetry. As above, we can project the 2-boundaries and obtain the Ammann–Beenker tiling as
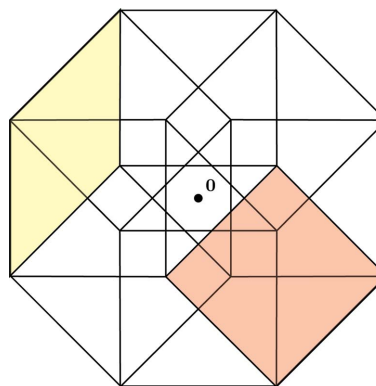

Figure 19
A projection of the Voronoi cell $V_{\mathbb{Z}^4}(\mathbf{0})$ into the $\perp$-space with two 2-boundaries indicated. The yellow rhombus corresponds to $\pi_\perp(Q(-+\bigcirc\bigcirc))$ and the red square to $\pi_\perp(Q(+\bigcirc+\bigcirc))$. In contrast with the Penrose tiling, the centre of the window is placed at the origin.
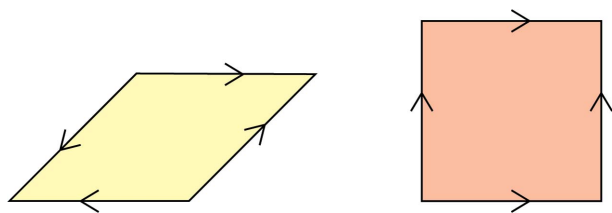
Figure 20
The decorated tiles for the Ammann–Beenker tiling. There are four different translation-equivalent rhombus tiles and eight different square tiles. They differ by a rotation by an integer multiple of $\pi/4$. In the case of the rhombus tiles, one has to decide on suitable representatives since the decorated tile possesses a rotation symmetry by π. We decided to pick up as the representatives the rhombus in the picture and its rotations by $\pi/4$, $\pi/2$ and $3\pi/4$.

$$\mathscr{T}_{\mathrm{AB}}(\mathbf{c}_\perp) = \left\{ \pi_\parallel(Q^*) \ : \ Q^* \text{ is a 2-boundary, } \mathbf{c}_\perp \in \pi_\perp(Q) \right\}. \tag{45}$$

We choose the vector $\mathbf{c}_\perp$ so that it does not belong to any 1-boundary of any Voronoi cell, similar to the Penrose case. In contrast with the Penrose tiling, we project the dual boundaries into the ∥-space, but this does not cause any difficulties. The ⊥-projection of the Voronoi cell with projections of two particular 2-boundaries is shown in Fig. 19. The area of the projection (which is an octagon) is $1 + \sqrt{2}$. Up to a translation, we have twelve different tiles – four rhombi and eight squares(!). This, perhaps surprising, fact follows from the decorations of the Ammann–Beenker tiles [see Baake & Grimm (2013) for further details]. Fig. 20 shows the tiles and their decorations.

As in the case of the Penrose tiling, we can determine all elementary polygons and obtain all possible vertex configurations as shown in Fig. 21.

Since there are no holes in this setting (as $\mathbb{Z}^4$ is self-dual as a lattice), the algorithm for determining the patch frequencies has to be modified as follows. One has to replace 'distinguishing between deep and shallow holes' in Step 1 with 'decorating the tiles', and in Step 3 one has to replace 'any shallow hole' with 'any vertex point', since there is only a single translation class. And, of course, in the last step, one has to divide by the accurate area of the window, in this case by
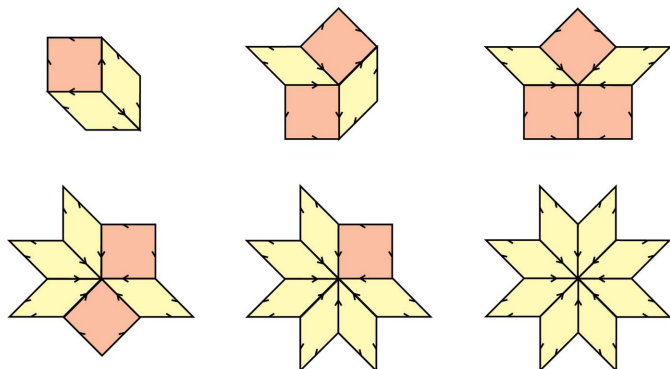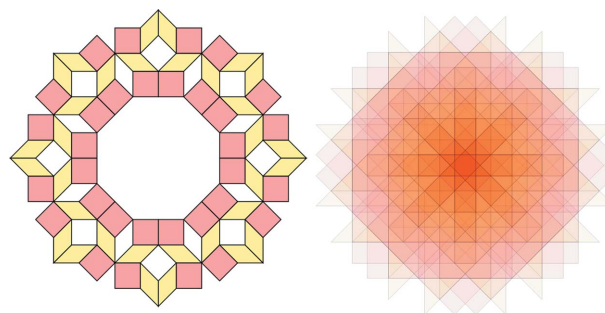

Figure 22
A 64-tile patch. Its frequency is $\nu_{64} = 29\lambda - 70 = \lambda^{-5}$.

Figure 23
A 104-tile patch. Its frequency is $\nu_{104} = 985 - 408\lambda = \lambda^{-8}$.

Figure 21
All allowed vertex configurations (up to rotations) within the Ammann–Beenker tiling displayed with decorations.

Figure 24
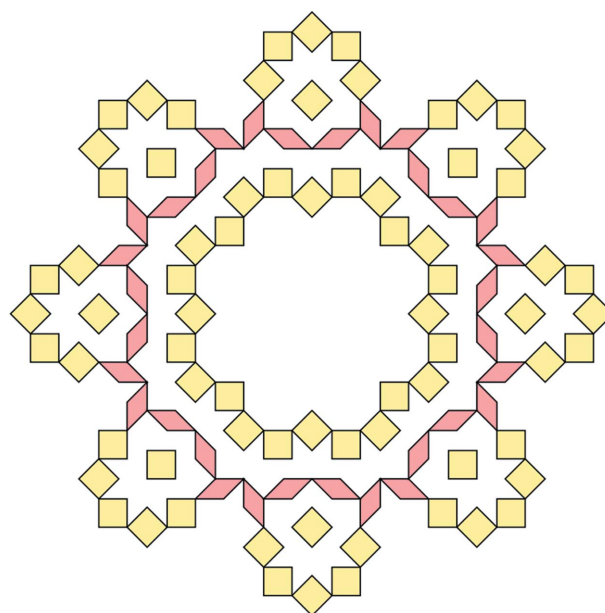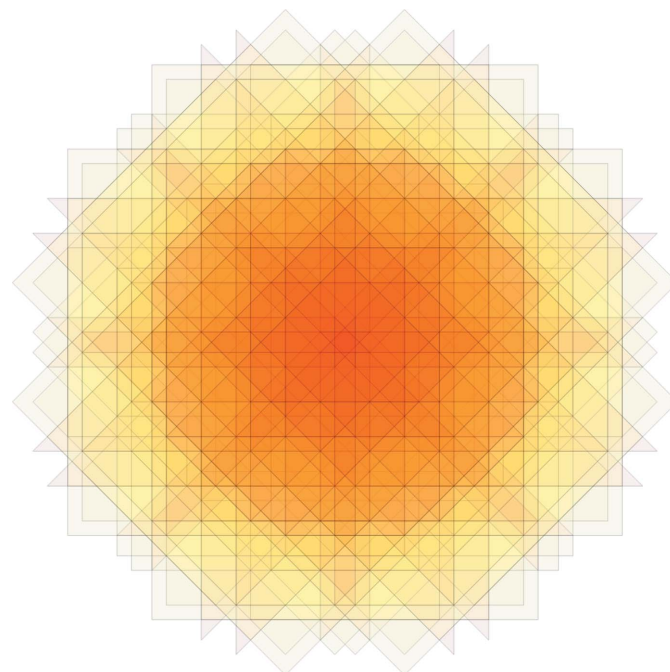The intersection of dual tiles of the patch from Fig. 23.

Figure 25
A 328-tile patch. Its frequency is $\nu_{328} = 985 - 408\lambda = \lambda^{-8}$.

Figure 26
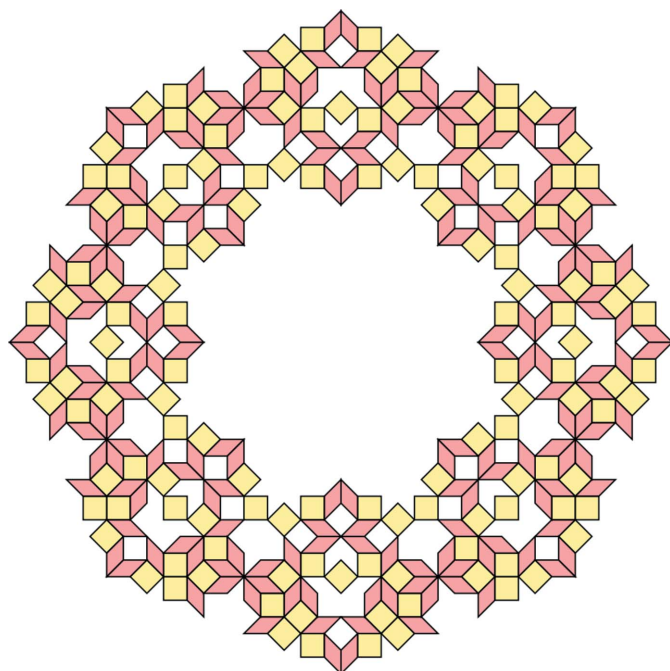The intersection of dual tiles of the patch from Fig. 25.

$1 + \sqrt{2}$. No other changes are needed. The patch frequencies are contained in the frequency module $\mathcal{M}_{\mathcal{T}_{AB}}$ which reads $\mathcal{M}_{\mathcal{T}_{AB}} = \frac{1}{2}\mathbb{Z}[\lambda]$ with $\lambda = 1 + \sqrt{2}$, the *silver mean* (Baake & Grimm, 2013, Example 7.9).

Figs. 22 to 26 show several patches of the Ammann–Beenker tiling which appear in Damanik *et al.* (2022), with their frequencies.

References

Baake, M. & Grimm, U. (2013). *Aperiodic Order*. Vol. 1, *A Mathematical Invitation*. Cambridge University Press.
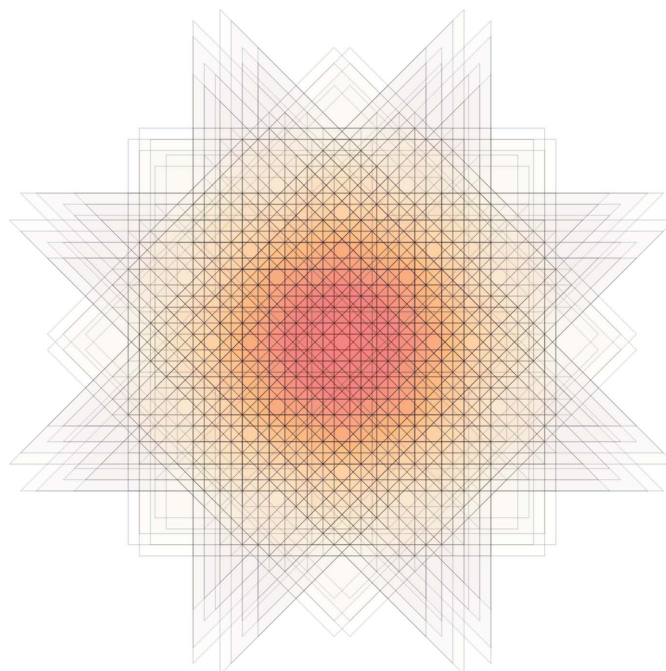Baake, M. & Joseph, D. (1990). *Phys. Rev. B*, **42**, 8091–8102.
Baake, M. B., Gemünden, B. & Oedingen, R. (1982). *J. Math. Phys.* **23**, 944–953.
Baake, M. D., Joseph, D. & Schlottmann, M. (1991). *Int. J. Mod. Phys. B*, **05**, 1927–1953.
Baake, M. P., Kramer, M., Schlottmann, M. & Zeidler, D. (1990). *Int. J. Mod. Phys. B*, **04**, 2217–2268.
Bruijn, N. G. de (1981a). *Indag. Math. Proced.* **84**, 39–52.
Bruijn, N. G. de (1981b). *Indag. Math. Proced.* **84**, 53–66.
Conway, J. & Sloane, N. J. A. (1999). *Sphere Packings, Lattices and Groups*, 3rd ed. New York: Springer.
Damanik, D., Embree, M., Fillman, J. & Mei, M. (2022). arXiv: 2209.01443.
Flicker, F., Simon, S. H. & Parameswaran, S. A. (2020). *Phys. Rev. X*, **10**, 011005.
Fujiwara, T. M., Arai, T., Tokihiro, T. & Kohmoto, M. (1988). *Phys. Rev. B*, **37**, 2797–2804.
Kepler, J. (1940). *Harmonices Mundi V*. In *Gesammelte Werke*, Band 6. Munich: Max Casper (Hrsg.) and C. H. Beck.
Keskiner, M. A. & Oktel, M. Ö. (2022). *Phys. Rev. B*, **106**, 064207.
Koecher, M. & Krieg, A. (2007). *Ebene Geometrie*, 3rd ed, p. 125. Berlin: Springer.
Kramer, P. & Schlottmann, M. (1989). *J. Phys. A Math. Gen.* **22**, L1097–L1102.
Lloyd, J., Biswas, S. H., Simon, S. A., Parameswaran, S. A. & Flicker, F. (2022). *Phys. Rev. B*, **106**, 094202.
Oktel, M. Ö. (2021). *Phys. Rev. B*, **104**, 014204.
Oktel, M. Ö. (2022). *Phys. Rev. B*, **106**, 024201.
Penrose, R. (1974). *Bull. Inst. Math. Appl.* **10**, 266–271.
Robinson, E. Jr (1996). *Trans. Am. Math. Soc.* **348**, 4447–4464.
Sutherland, I. E. & Hodgman, G. W. (1974). *Commun. ACM*, **17**, 32–42.
Zobetz, E. & Preisinger, A. (1990). *Acta Cryst.* A**46**, 962–970.